



Half-Sandwich $\text{LaB}_n^{-/0}$ ($n = 14\text{--}17$): π Dually Aromatic Lanthanide Boride Complexes with Multicenter Fluxional Bonds

Xiao-Qin Lu¹ · Zhihong Wei¹ · Si-Dian Li¹

Received: 28 September 2020 / Accepted: 17 April 2021

© The Author(s), under exclusive licence to Springer Science+Business Media, LLC, part of Springer Nature 2021

Abstract

Novel lanthanide boride complexes with unique structural and bonding patterns have been observed in recent experiments. Based on extensive first-principles theory calculations, we predict herein the possible existence of half-sandwich C_{2v} LaB_{14}^- (**1**), C_1 LaB_{15} (**2**), C_{5v} LaB_{16}^- (**3**), and C_s LaB_{17} (**4**) which all contain a La center coordinated by a bowl-like B_n ligand ($n = 14\text{--}17$). Detailed bonding analyses indicate that effective d-p coordination interactions exist between the La center and B_n ligand, making these half-sandwich complexes π dually aromatic in nature. Energy decomposition analyses reveal that electrostatic (50.2%) and covalent (49.8%) interactions contribute almost equally to the overall attraction in LaB_{14}^- (**1**), with the La centre serving as both electron donor and acceptor. Molecular dynamics simulations show that both LaB_{14}^- (**1**) ($\text{La}[\text{B}_4\text{B}_{10}]^-$) and LaB_{17} (**4**) ($\text{La}[\text{B}\text{B}_5\text{B}_{11}]$) with multicenter fluxional bonds behave like Wankel motors at finite temperatures.

Keyword First-principles theory · Lanthanide boride complexes · Half-sandwich complexes · Fluxional bonds · π Dual aromaticity

Introduction

Molecular rotors have attracted widespread attention in chemistry and enabled a wealth of applications in gas phases [1, 2], solutions [1, 3], crystals [1, 4], ferroelectric molecules [5], and on surfaces [1, 6]. It is well known that boron has a rich chemistry characterized with delocalized multicenter-two-electron (mc-2e) bonds in both bulk allotropes and polyhedral molecules due to its prototypical electron deficiency [7]. Over the past two decades, persistent joint photoelectron spectroscopy (PES) and first-principles theory (FPT) investigations have unveiled an unexpectedly wide range of size-selected boron clusters ($\text{B}_n^{-/0}$) from planar or quasi-planar structures ($n = 3\text{--}38$, 41, and 42) to cage-like borospherenes D_{2d} $\text{B}_{40}^{-/0}$ and C_3/C_2 B_{39}^- [8–12]. Joint ion mobility experiment and density functional theory (DFT) calculations indicated that

monocationic boron clusters B_n^+ possess planar or quasi-planar structures with n up to 15 and double-ring (DR) tubular geometries in the size range between $n = 16\text{--}25$ [13]. The domain of flat boron clusters is governed by the localized two-center-two-electron (2c-2e) σ -bonds on the periphery and delocalized multicenter mc-2e σ and π bonds over the molecular moieties. Such a bonding pattern results in unique molecular dynamics and structural fluxionalities in C_{2v} B_{11}^- , C_{2v} B_{13}^+ , C_s B_{15}^+ , C_s B_{18}^{2-} , C_{2v} B_{19}^- , C_{2v} B_{20}^- , and C_{2v} B_{20}^{2-} which have been proposed to be Wankel motors [14–20]. These molecular motors consist of a small inner wheel that rotates constantly in an outer bearing at finite temperatures with extremely low-energy barriers on the potential energy surfaces.

Perfect transition-metal-centered monocyclic boron wheel clusters D_{8h} CoB_8^- , D_{9h} RuB_9^- , and D_{10h} TaB_{10}^- were observed in experiments [21, 22]. Larger metal-doped CoB_{12}^- and RhB_{12}^- complexes with a B_{12} ligand were later confirmed to have half-sandwich structures [23]. A family of transition-metal-centered DR tubular MnB_{16}^- , CoB_{16}^- , RhB_{18}^- and TaB_{20}^- were observed in PES measurements [24–27], with TaB_{20}^- as a tubular molecular rotor with the low energy barrier of 1.13 kcal mol⁻¹. Interestingly, molecular dynamics

✉ Zhihong Wei
weizhihong@sxu.edu.cn

✉ Si-Dian Li
lisidian@sxu.edu.cn

¹ Institute of Molecular Science, Shanxi University,
Taiyuan 030006, China

simulation indicates that the half-sandwich C_s NiB_{11}^- ($[\text{Ni}(\text{B}_3\text{C}\text{B}_8)]^-$) also behaves like a Wankel motor at room temperature, with the B_3 inner ring rotating almost freely inside the B_8 outer bearing facilitated by fluxional bonding interactions in between [28]. Fluxional bonds (FBs) which form and break constantly in concerted mechanisms under certain conditions were firstly proposed by our group in planar C_{2v} B_{19}^- , tubular C_s $\text{Ta}@\text{B}_{20}^-$, and cage-like C_3/C_2 B_{39}^- [29] and late extended to half-sandwich C_s MB_{18}^- ($\text{M} = \text{K}, \text{Rb}, \text{and Cs}$) [30] and cage-like bullvalene ($\text{C}_{10}\text{H}_{10}$) and its analogs [31]. A family of inverse sandwich di-lanthanide boron complexes D_{7h} La_2B_7^- , D_{8h} La_2B_8 and D_{9h} La_2B_9^- were recently discovered in PES measurements [32, 33]. Tri-La-doped inverse triple-decker C_{2v} $\text{La}_3\text{B}_{14}^-$ and cage-like metallo-borospherene D_{3h} $\text{La}_3\text{B}_{18}^-$ were both observed in recent PES experiments [34, 35]. Our group predicted recently the smallest lanthanide boride inverse sandwich tubular molecular rotor C_{2h} La_2B_{18} which possesses a B_2 -bar rotating almost freely inside a B_{18} DR tube around it at room temperature via multicenter fluxional bonds and the smallest core-shell-like metallo-borospherene La_3B_{18} which contains a B_2 core with unique donor-acceptor duality [36, 37].

Based on extensive global minimum (GM) searches and first-principles theory calculations, we predict herein the possibility of a series of mono-La-doped half-sandwich boron complexes C_{2v} LaB_{14}^- (1), C_1 LaB_{15} (2), C_{5v} LaB_{16}^- (3), and C_s LaB_{17} (4) which are stabilized by effective (d-p) σ , (d-p) π , and (d-p) δ interactions between the La center and bowl-like B_n ligands ($n = 14\text{--}17$). Such bonding patterns render π dual aromaticity to these half-sandwich complexes in which both LaB_{14}^- (1) ($[\text{La}(\text{B}_4\text{C}\text{B}_{10})]^-$) and LaB_{17} (4) ($[\text{La}(\text{B}_5\text{C}\text{B}_{11})]^-$) are typical Wankel motor molecules at finite temperatures with multicenter FBs between a small inner wheel (B_4 or B_5) and an outer bearing (B_{10} or B_{11}).

Theoretical Procedure

Extensive global minimum (GM) searches were performed on LaB_{14}^- , LaB_{15} , LaB_{16}^- , and LaB_{17} using the TGmin2 code [38] at the DFT level, in conjunction with manual structural constructions based on the previously reported $\text{B}_n^{-/0/+}$ clusters ($n = 14, 17$) [8, 12]. More than 2000 tried structures were explored for each species at PBE/TZVP level. Low-lying isomers were then fully re-optimized at PBE0 [39] and TPSSH [40] levels with the 6-311 + G* basis set [41] for B and Stuttgart relativistic small-core pseudopotential for La [42, 43] using the Gaussian 09 program suite [44], with vibrational frequencies checked to make sure all the low-lying isomers obtained are true

minima of the systems. Single-point energies of the five lowest-lying isomers were further refined at the PBE0 geometries using the CCSD(T) method [45–47] implemented in MOLPRO [48]. Special attention was paid to locate both the intermediate (IM) and transition states (TS) of LaB_{14}^- (1) which turns out to have a much more complicated potential energy surface than LaB_{17} (4). Both forward and backward reaction paths were followed by integrating the intrinsic reaction coordinates of LaB_{14}^- and LaB_{17} . Detailed bonding analyses were performed on the GMs, TSs, and IMs of the concerned species using the adaptive natural density partitioning (AdNDP) approach at PBE0 level [49] which recovers both the localized and delocalized bonds in the concerned systems. Natural bonding orbital (NBO) analyses were performed using the NBO 6.0 program [50]. Born–Oppenheimer molecular dynamics (BOMD) simulations were performed on LaB_{14}^- and LaB_{17} for 30 ps at different temperatures from 300 to 1000 K using the CP2K software package [51]. Detailed energy decomposition analysis – natural orbitals for chemical valence (EDA-NOCV) [52–54] was performed using the ADF program [55] at PBE0/TZP-ZORA level to quantitatively elucidate the bonding mechanisms between the B_{14}^{2-} and La^+ fragments in LaB_{14}^- (1). The zero-order regular approximation [56–58] was applied to account for the scalar relativistic effects. The frozen core approximation was not employed in these computations. In the EDA analysis, the interaction energy (ΔE_{int}) between two fragments is decomposed into electrostatic interaction energy (ΔE_{elstat}), Pauli repulsion (ΔE_{Pauli}), and orbital interaction energy (ΔE_{orb}) in Eq. 1. The fragments interaction with the smallest orbital interaction energy is best suited to describe the bonding scheme of the system (Fig. 1).

$$\Delta E_{\text{int}} = \Delta E_{\text{elstat}} + \Delta E_{\text{Pauli}} + \Delta E_{\text{orb}} \quad (1)$$

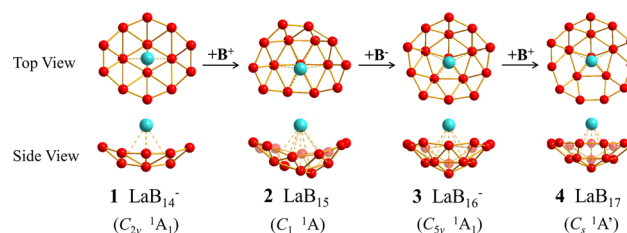


Fig. 1 Optimized structures of half-sandwich C_{2v} LaB_{14}^- (1), C_1 LaB_{15} (2), C_{5v} LaB_{16}^- (3), and C_s LaB_{17} (4) at PBE0/6-311 + G(d) level

Results and Discussion

Structures and Stabilities

Using the experimentally observed quasi-planar C_s B_{14}^- [8] as ligand, the half-sandwich C_{2v} LaB_{14}^- (**1**) was obtained as the GM of the monoanion with the large HOMO–LUMO gap of $\Delta E_{\text{gap}} = 2.42$ eV. It is 0.27, 0.25, 0.27 eV more stable than the second lowest-lying isomer C_s LaB_{14}^- at PBE0, TPSSh, and CCSD(T) levels, respectively (Fig. S1). Other isomers are found to lie much higher in energy (> 0.68 eV) than the GM at CCSD(T). LaB_{14}^- (**1**) contains a B_4 rhombic inside a B_{10} outer bearing and can be better formulated as C_{2v} $\text{La}[\text{B}_4\text{C}\text{B}_{10}]^-$. The B_4 rhombic in it possesses the average La–B distance of $r_{\text{La-B}} = 2.64$ Å which is obviously shorter than the corresponding value of $r_{\text{La-B}} = 2.92$ Å between La and the ten B atoms in outer bearing. Detailed NBO analyses on closed-shell LaB_{14}^- (**1**) show that the La center possesses the natural atomic charge of $q_{\text{La}} = +1.02$ |e|, electronic configuration of La $[\text{Xe}]4f^{0.22}5d^{1.69}6s^{0.09}$, and total Wiberg bond order of $\text{WBI}_{\text{La}} = 3.27$. Obviously, the central La atom in LaB_{14}^- (**1**) donates its $6s^2$ electrons almost completely to the B_{14} ligand, while, in return, accepts about one electron in its 5d orbital via effective B_{14} (p) \rightarrow La (5d) back-donation, resulting in a NBO natural charge distribution of $\text{La}^+-\text{B}_{14}^{2-}$ in LaB_{14}^- (**1**). Extensive BOMD simulations reveal the typical fluxional behavior of LaB_{14}^- (**1**) at 1000 K (Video S1). During the simulations, LaB_{14}^- (**1**) maintains its basic half-sandwich structure, with the B_4 rhombus rotating constantly inside the B_{10} outer bearing in a concerted mechanism. One intermediate C_s LaB_{14}^- with the relative energy of 6.24 kcal/mol and two degenerate chiral transition states C_1 LaB_{14}^- and C_1' LaB_{14}^- with activation energy of $\Delta E_a = 6.40$ kcal/mol are located on the potential energy surface of LaB_{14}^- (Fig. 2a). The energy barriers of $\Delta E_a = 6.40$ kcal/mol from C_{2v} GM to C_1 TS and $\Delta E_a = 0.16$ kcal/mol from the C_s IM to either C_1 TS or C_1' TS are not overwhelming, which, as shown in Video S1, can be overcome by thermo-excitations at 1000 K. There exists thus a pseudo-rotation between the B_4 rhombus and the B_{10} outer bearing in LaB_{14}^- (**1**) with the rotational angle of 9° in each step. A chiral conversion via the pseudo-rotation is achieved on the pathway between the two degenerate enantiomers TS1 and TS1' in LaB_{14}^- (**1**). The specific multicenter fluxional bonds highlighted in Fig. 2 will be discussed in details in the following section.

Adding one B^+ monocation in LaB_{14}^- (**1**) generates the distorted half-sandwich C_1 LaB_{15} (**2**) ($\text{La}[\text{B}_5\text{C}\text{B}_{10}]$) which is the GM of neutral LaB_{15} lying 0.04 eV more stable than the second lowest-lying C_s LaB_{15} at CCSD(T) (Fig. S2). The four lowest-lying half-sandwich isomers of LaB_{15}

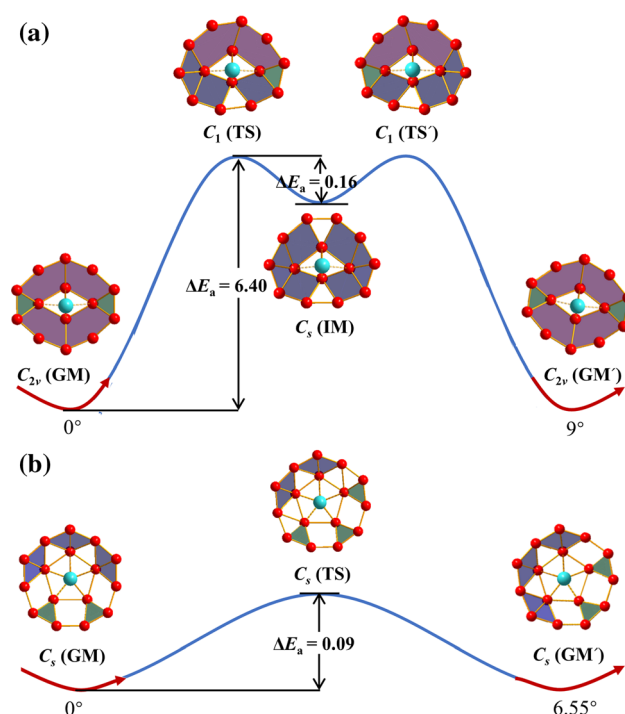


Fig. 2 **a** Bonding fluctuations in C_{2v} LaB_{14}^- (**1**) ($2\ 3c\text{--}2e\ \sigma + 4\ 5c\text{--}2e\ \sigma$) via two transition states C_1 LaB_{14}^- (TS and TS') ($1\ 3c\text{--}2e\ \sigma + 3\ 4c\text{--}2e\ \sigma + 2\ 5c\text{--}2e\ \sigma$) and one intermediate C_s LaB_{14}^- ($6\ 4c\text{--}2e\ \sigma$) and **b** bonding fluctuations in C_s LaB_{17} (**4**) ($2\ 3c\text{--}2e\ \sigma + 3\ 4c\text{--}2e\ \sigma$) via the transition state C_s LaB_{17} ($3\ 3c\text{--}2e\ \sigma + 2\ 4c\text{--}2e\ \sigma$), with the $3c\text{--}2e$, $4c\text{--}2e$, and $5c\text{--}2e\ \sigma$ bonds highlighted in green, blue, and purple, respectively. The activation energies ΔE_a are indicated in kcal/mol at CCSD(T) level

lying within 0.14 eV at CCSD(T) in relative energies (Fig. S2) are practically degenerate species which may coexist in experiments.

Extensive global searches indicate that, as shown in Fig. S3, LaB_{16}^- strongly favors the high-symmetry half-sandwich C_{5v} LaB_{16}^- (**3**) over its singlet and triplet tubular counterparts, in sharp contrast to the experimentally observed DR tubular D_{8d} CoB_{16}^- and C_{4v} MnB_{16}^- [24, 25] due to size effect. La possesses a much larger atomic radius (1.83 Å) than both Co (1.25 Å) and Mn (1.27 Å) [59]. The C_{5v} GM (**3**) contains a $\text{B}\text{C}\text{B}_5$ pentagonal pyramid inside the B_{10} outer bearing in a close-packed motif ($\text{La}[\text{B}\text{C}\text{B}_5\text{C}\text{B}_{10}]^-$). It lies 0.08, 0.06, and 0.16 eV lower than the second (C_s), third (C_s), and fourth (C_s) lowest-lying half-sandwich isomers at CCSD(T) and 1.48 and 1.96 eV lower than the distorted singlet and triplet DR tubular C_{2v} isomers at PBE0, respectively (Fig. S3). LaB_{16}^- (**3**) possesses the optimized La–B distances of $r_{\text{La-B}} = 2.98$ Å between La and the central B atom, $r_{\text{La-B}} = 2.76$ Å between La and the five B atoms on the B_5 pentagon, and $r_{\text{La-B}} = 2.85$ Å (in average) between La and the ten B atoms on the B_{10} outer bearing. Its La center possesses the natural atomic charge of $q_{\text{La}} = +1.18$ |e|,

electronic configuration of La $[\text{Xe}]4f^{0.32}5d^{1.44}6s^{0.09}$, and total Wiberg bond order of $\text{WBI}_{\text{La}} = 3.21$, similar to the situation in LaB_{14}^- (1) discussed above.

Introducing one B^+ cation into the B_{10} outer bearing of LaB_{16}^- (3) results in half-sandwich C_s LaB_{17} (4) ($\text{La}[\text{B}\odot\text{B}_5\odot\text{B}_{11}]$), the well-defined GM of neutral LaB_{17} which is 0.54 eV more stable than the second lowest-lying half-sandwich isomer C_s LaB_{17} (Fig. S4). LaB_{17} (4) contains a quadrilateral B_4 hole as structural defect between the B_5 inner ring and B_{11} outer bearing to facilitate the fluxional behavior of the neutral cluster. The La center possesses the natural atomic charge of $q_{\text{La}} = 1.34$ lel, electronic configuration of La $[\text{Xe}]4f^{0.22}5d^{1.36}6s^{0.09}$, and total Wiberg bond order of $\text{WBI}_{\text{La}} = 2.92$, respectively. Extensive BOMD simulations indicate that, with the small energy barrier of 0.0039 eV (0.09 kcal/mol) between the C_s TS and C_s GM at CCSD(T), LaB_{17} (4) behaves like a Wankel rotor in pseudo-rotations at room temperature (300 K) (Video S2), with the $\text{B}\odot\text{B}_5$ pentagonal pyramid rotating almost freely inside the B_{11} outer bearing with the rotational angle of 6.55° in each step (Fig. 2b). The C_s TS of LaB_{17} with the imaginary vibrational frequency of $93i$ cm^{-1} appears to have the same symmetry as the GM LaB_{17} (4).

Bonding Analyses

Detailed AdNDP bonding analyses in Fig. 3a indicate that LaB_{14}^- (1) possesses 10 2c-2e σ bonds on the B_{10} outer bearing, 1 4c-2e σ bond on the inner B_4 rhombus, 2 3c-2e σ bonds and 4 5c-2e σ bonds between the B_4 rhombus and B_{10} outer bearing with the occupation number of $\text{ON} = 1.86\text{--}1.91$ lel in the first row, in an overall symmetry of C_{2v} . The second row contains 1 5c-2e $\text{B}_4(\pi)\text{-La}(d_\sigma)$ bond between La and the B_4 rhombus under it with $\text{ON} = 1.97$ lel, 3 15c-2e $\text{B}_{14}(\pi)\text{-La}(d_{\pi/\sigma})$ bonds over the half-sandwich structure with $\text{ON} = 2.00$ lel, and 2 15c-2e $\text{B}_{14}(\pi)\text{-La}_2(d_\delta)$ bonds with $\text{ON} = 2.00$ lel. The 5c-2e (p-d) π bond and three 15-2e (p-d) π bonds in the second row form two concentric π -systems matching the $4n + 2$ π -aromatic rule with $n = 0$ and 1, respectively, rendering π dual aromaticity to the half-sandwich system. The two totally delocalized (p-d) δ bonds at the end help to further stabilize the monoanion. Interestingly, both the intermediate C_s LaB_{14}^- and transition state C_1 LaB_{14}^- exhibit very similar bonding patterns (Fig. S5a and S5b) with that of C_{2v} GM (Fig. 3a), with the main difference occurring at the six delocalized σ -bonds between the B_4 rhombus and B_{10} outer bearing, while all the other σ and π bonds remain basically unchanged. In specific, the 2 3c-2e σ + 4 5c-2e σ bonds in the GM (Fig. 3a) have been transferred into 1 3c-2e σ + 3 4c-2e σ + 2 5c-2e σ bonds in the TS (Fig. S5a) and 6 4c-2e σ bonds in the IM (Fig. S5b). Such a 2 3c-2e σ + 4 5c-2e σ

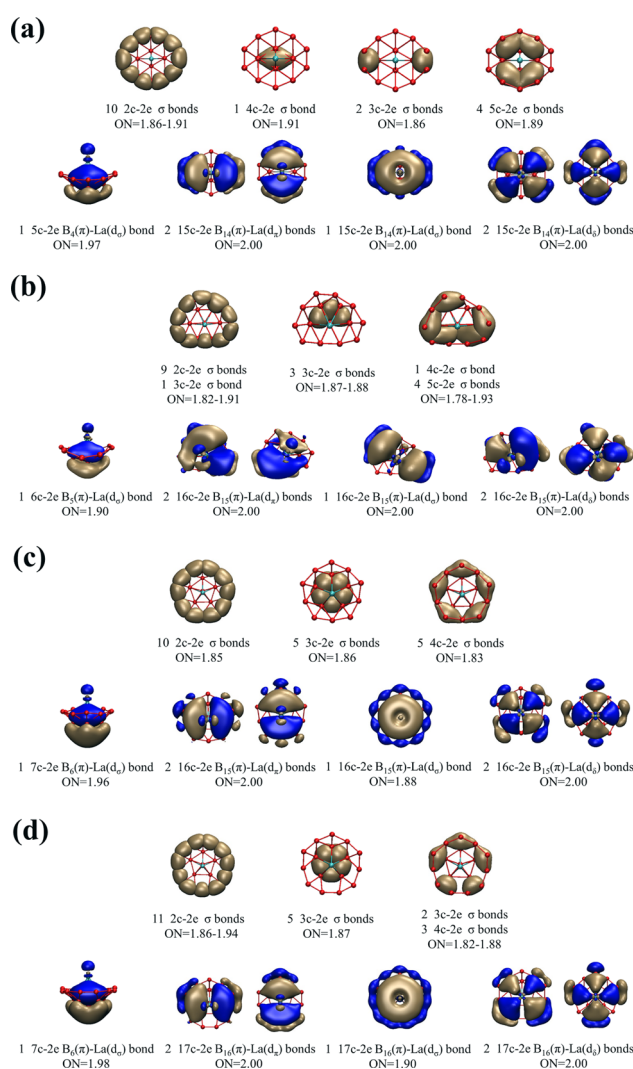


Fig. 3 AdNDP bonding patterns of **a** LaB_{14}^- (1), **b** LaB_{15}^- (2), **c** LaB_{16}^- (3), and **d** LaB_{17} (4), with the occupation numbers (ONs) indicated

(GM) \rightarrow 1 3c-2e σ + 3 4c-2e σ + 2 5c-2e σ (TS) \rightarrow 6 4c-2e σ (IM) \rightarrow 1 3c-2e σ + 3 4c-2e σ + 2 5c-2e σ (TS) \rightarrow 2 3c-2e σ + 4 5c-2e σ (GM) bonding fluctuation repeats itself in the pseudo-rotation process of the half-sandwich molecular rotor. The close-packed C_1 LaB_{15} (2) also appears to be π dually aromatic, in nature, with 1 6c-2e (d-p) π bond at the center and 3 16c-2e (d-p) π bonds over the distorted half-sandwich structure (Fig. 3b).

The high-symmetry LaB_{16}^- (3) possesses a similar but more elegant bonding pattern. As shown in Fig. 3c, it contains 10 2c-2e σ bonds on the B_{10} outer bearing, 5 3c-2e σ bonds on the $\text{B}\odot\text{B}_5$ pentagonal pyramid, and 5 4c-2e σ bonds between the B_5 middle ring and B_{10} outer ring in the first row and 1 7c-2e $\text{B}_6(\pi)\text{-La}(d_\sigma)$ bond between La and the $\text{B}\odot\text{B}_5$ pentagonal pyramid, 3 16c-2e (d-p) π bonds, and 2 16c-2e (d-p) δ bonds between La and the $\text{B}_5\odot\text{B}_{10}$

double ring motif in the second row, in an overall symmetry of C_{5v} , again rendering π dual aromaticity to the monoanion.

Both the fluxional C_s LaB_{17} (**4**) and its transition state C_s LaB_{17} appear to well inherit the main bonding characteristics of C_{5v} LaB_{16}^- (**3**) (Fig. 3d and Fig. S6). The main bonding difference between them occurs in the five delocalized σ bonds which fluctuate constantly at room temperature between the B_5 middle ring and the B_{11} outer bearing, with 2 3c-2e σ + 3 4c-2e σ bonds in the C_s GM (Fig. 3d) transferred into 3 3c-2e σ + 2 4c-2e σ bonds in C_s TS (Fig. S6). The 2 3c-2e σ + 3 4c-2e σ (GM) \rightarrow 3 3c-2e σ + 2 4c-2e σ (TS) \rightarrow 2 3c-2e σ + 3 4c-2e σ (GM) bonding fluctuation shown facilitates the fluxional behaviors of LaB_{17} (**4**).

Detailed EDA-NOCV analyses [52–54] shed quantitative insights into the nature of the bonding interactions in these half-sandwich complexes, as demonstrated for LaB_{14}^- (**1**) in Fig. 4. With the smallest orbital interaction energy of $\Delta E_{\text{orb}} = -300.2$ kcal/mol, the La^+ and B_{14}^{2-} fragments interaction is best suited to describe the bonding scheme of LaB_{14}^- (**1**) in various schemes considered. Such $\text{La}^+ \dots \text{B}_{14}^{2-}$ scheme is well in line with the NBO natural charge distribution of $\text{La}^+ \text{--} \text{B}_{14}^{2-}$ in LaB_{14}^- (**1**). The bonding molecular orbitals (MOs) $8a_2$, $27a_1$, $26a_1$, $14b_2$ and $14b_1$ which represent covalent interactions between the La^+ ligand and B_{14}^{2-} ligand are connected with the corresponding fragmental orbitals by red lines in Fig. 4, with

the orbital compositions listed in Table S1. The MO $8a_2$ is mainly composed of contributions from the occupied $3a_2$ of La^+ with $d_{x^2-y^2}$ character and vacant $6a_2$ of B_{14}^{2-} with π feature. The MO $27a_1$ is a linear combination of the occupied $14a_1$ of B_{14}^{2-} with π feature and vacant $15a_1$ and $16a_1$ of La^+ with d_{z^2} and d_{xy} characters, respectively. The $26a_1$ is mainly a combination of the occupied $13a_1$ of B_{14}^{2-} with π feature and vacant $15a_1$ of La^+ with d_{z^2} feature. The $14b_2$ and $14b_1$ mainly originate from the occupied $8b_2$ and $8b_1$ of B_{14}^{2-} with π character and vacant $7b_2$ and $7b_1$ of La^+ with d_{xz} and d_{yz} characters, respectively. There exists a strong charge transfer (+ 1.02 |e|) from La to B_{14} , resulting in the $\text{La}^+ \text{--} \text{B}_{14}^{2-}$ pairwise interaction in LaB_{14}^- (**1**).

We analysed the $\text{La}^+ \text{--} \text{B}_{14}^{2-}$ interaction by the decomposition of the orbital terms into pairwise contributions, as shown in Table 1. The interaction energy ΔE_{int} consists of Pauli repulsion ΔE_{Pauli} , Coulombic attraction ΔE_{elstat} , and orbital interaction ΔE_{orb} , with almost equal covalent contribution (50.2%) and electrostatic contribution (49.8%). The decompositions of the orbital interactions ΔE_{orb} into pairwise contributions between occupied and vacant MOs of the fragments provide quantitative insight into the charge flow. There exist five major terms $\Delta E_1 \sim \Delta E_5$ associated with the deformation densities $\Delta\rho_1 \text{--} \Delta\rho_5$, respectively. The remaining terms contribute < 10% to the total orbital interactions. The color code of the deformation densities indicates the direction of the charge flow from

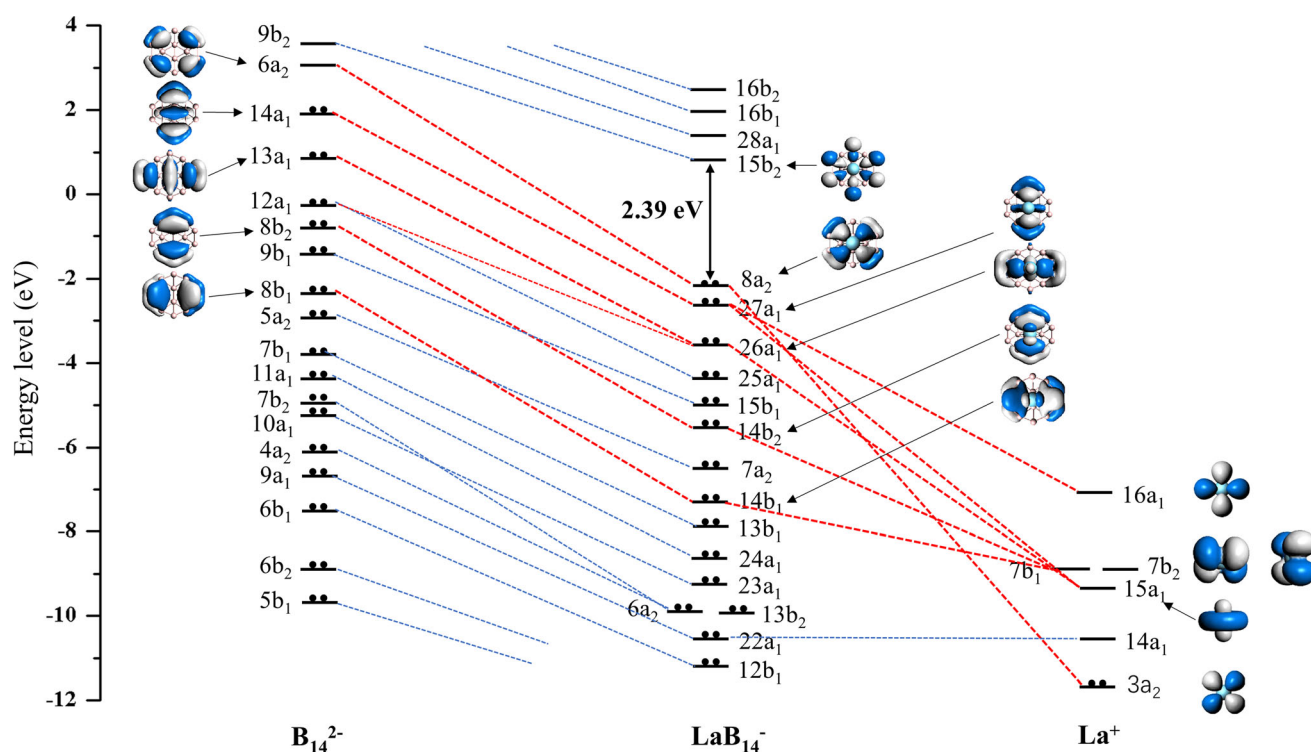


Fig. 4 Bonding scheme of C_{2v} LaB_{14}^- (**1**) using the fragments La^+ and B_{14}^{2-} as interacting species at PBE0/TZP-ZORA level

Table 1 EDA-NOCV analysis of the LaB_{14}^- (**1**) at PBE0/TZP-ZORA level using the fragments La^+ and B_{14}^{2-} as interacting species. All energy values are in kcal mol^{-1}

Energy terms	Orbital interaction	$\text{La}^+ + \text{B}_{14}^{2-}$
ΔE_{int}		- 377.0
ΔE_{Pauli}		225.4
$\Delta E_{\text{elstat}}^{\text{[a]}}$		- 302.2 (50.2%)
$\Delta E_{\text{orb}}^{\text{[a]}}$		- 300.2 (49.8%)
$\Delta E_{\text{orb}(1)}^{\text{[b]}}$	$[\text{La}^+ (\text{d})] \rightarrow [\text{B}_{14}^{2-} (\text{p})]$	- 142.8 (47.6%)
$\Delta E_{\text{orb}(2)}^{\text{[b]}}$	$[\text{La}^+ (\text{d})] \leftarrow [\text{B}_{14}^{2-} (\text{p})]$	- 44.2 (14.7%)
$\Delta E_{\text{orb}(3)}^{\text{[b]}}$	$[\text{La}^+ (\text{d})] \leftarrow [\text{B}_{14}^{2-} (\text{p})]$	- 35.2 (11.7%)
$\Delta E_{\text{orb}(4)}^{\text{[b]}}$	$[\text{La}^+ (\text{d})] \leftarrow [\text{B}_{14}^{2-} (\text{p})]$	- 26.9 (9.0%)
$\Delta E_{\text{orb}(5)}^{\text{[b]}}$	$[\text{La}^+ (\text{d})] \leftarrow [\text{B}_{14}^{2-} (\text{p})]$	- 23.0 (7.7%)
$\Delta E_{\text{orb}(\text{rest})}^{\text{[b]}}$		- 28.1 (9.4%)

^aThe value in parentheses gives the percentage contribution to the total attractive interactions ($\Delta E_{\text{elstat}} + \Delta E_{\text{orb}}$)

^bThe value in parentheses gives the percentage contribution to the total orbital interactions

red \rightarrow blue, as shown in Fig. S7. The strongest orbital interaction $\Delta E_{\text{orb}(1)}$ (47.6%) arises mainly from the $[\text{La}^+ (\text{d})] \rightarrow [\text{B}_{14}^{2-} (\text{p})]$ donation in which the La^+ centre serves as a donor to the B_{14}^{2-} ligand, while the relatively weaker orbital interaction $\Delta E_{\text{orb}(2-5)}$ (43.1%) originates from the $[\text{La}^+ (\text{d})] \leftarrow [\text{B}_{14}^{2-} (\text{p})]$ back-donation where the La^+ centre is an acceptor from the B_{14}^{2-} ligand (Table 1).

Spectral Simulations

Finally, we computationally simulate the IR, Raman, and PES spectra of LaB_{14}^- (**1**) in Fig. 5 to facilitate its future infrared-photodissociation (IR-PD) or PES spectroscopic characterizations. Its major IR bands occur at 597(b_1), 814(b_2), 1117(b_1) and 1262(b_1) cm^{-1} , with the corresponding Raman active vibrations located at 679(a_1), 1171(a_1) and 1381(a_1) cm^{-1} , respectively. The calculated PES spectrum of LaB_{14}^- (**1**) exhibits major spectral features at 2.85, 3.05, 3.92, 4.54, 4.99–5.81 and 6.21 eV, respectively, which correspond to vertical electronic transitions from the ground state of the anion to the ground and excited states of the neutral at the ground-state geometry of the anion. The simulated IR, Raman and PES spectra of LaB_{16}^- (**3**) are depicted in Fig. S8 and IR, Raman and UV-vis spectra of LaB_{17} (**4**) shown in Fig. S9.

Conclusions

In summary, we have presented in this work a comprehensive first-principles theory investigation on a series of half-sandwich lanthanide boride clusters including C_{2v}

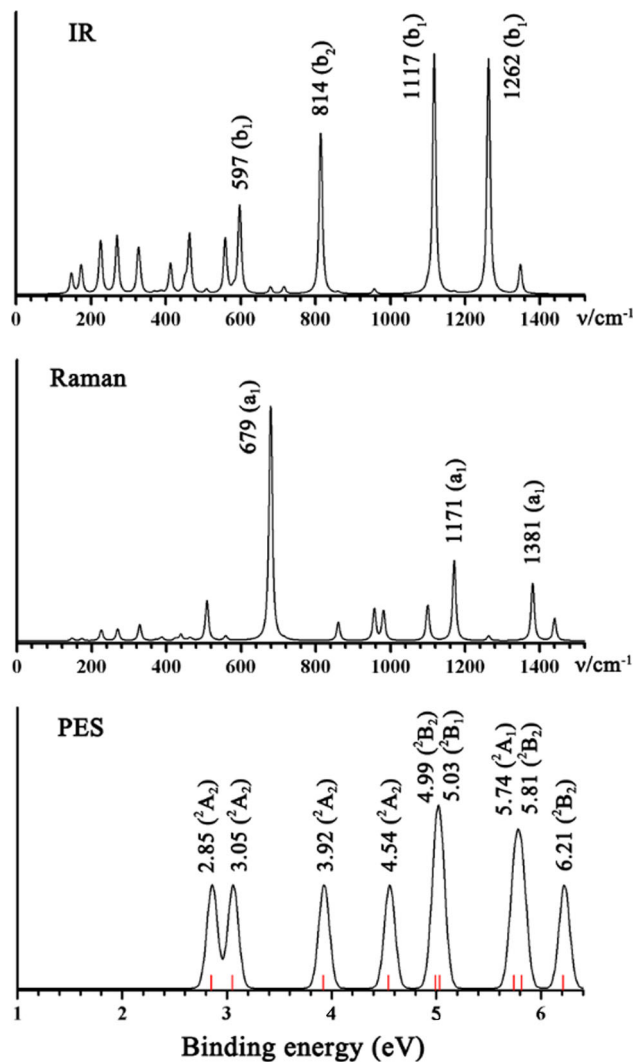


Fig. 5 Simulated IR, Raman and PES spectra of LaB_{14}^- (**1**) at PBE0/6-311 + G(d) level

LaB_{14}^- (**1**), C_1 LaB_{15} (**2**), C_{5v} LaB_{16}^- (**3**), and C_s LaB_{17} (**4**) which all appear to be π dually aromatic in nature. In particular, C_{2v} LaB_{14}^- (**1**) and C_s LaB_{17} (**4**) prove to be typical Wankel motor molecules at finite temperatures in concerted mechanisms with low energy barriers. The fluxional behaviors of these half-sandwich complexes originate from the multicenter σ -FBs in them between the inner wheel (B_4 or B_5) and outer bearing (B_{10} or B_{11}). Such stable lanthanide-boron binary species may be produced and characterized in PES or IR-PD experiments in gas phases. More lanthanide-doped complexes may be explored in both experiments and theory to form novel nanostructures with unique magnetic, electronic, and catalytic properties.

Supplementary Information The online version contains supplementary material available at <https://doi.org/10.1007/s10876-021-02072-x>.

Acknowledgements The work was supported by the National Natural Science Foundation of China (21720102006 and 21973057 to S.-D. Li).

Declarations

Conflict of interest All the authors of this paper have no conflict of interest.

References

- G. S. Kottas, L. I. Clarke, D. Horinek, and J. Michl (2005). *Chem. Rev.* **105**, 1281.
- H. Isobe, H. K. Nakamura, S. Hitosugi, S. Sato, H. Tokoyama, H. Yamakado, K. Ohno, and H. Kono (2015). *Chem. Sci.* **6**, 2746.
- S. P. Fletcher, F. Dumur, M. M. Pollard, and B. L. Feringa (2005). *Science* **310**, 80.
- C. Lemouchi, K. Iliopoulos, L. Zorina, S. Simonov, P. Wzietek, T. Cauchy, A. Rodríguez-Fortea, E. Canadell, J. Kaleta, J. Michl, D. Gindre, M. Chrysos, and P. Batail (2013). *J. Am. Chem. Soc.* **135**, 9366.
- T. Akutagawa, H. Koshinaka, D. Sato, S. Takeda, S.-I. Noro, H. Takahashi, R. Kumai, Y. Tokura, and T. Nakamura (2009). *Nat. Mater.* **8**, 342.
- D. Horinek and J. Michl (2003). *J. Am. Chem. Soc.* **125**, 11900.
- F. A. Cotton, G. Wilkinson, C. A. Murillo, and M. Bochmann (1999). *Advanced Inorganic Chemistry*, Wiley, New York, 6th ed.
- H. J. Zhai, B. Kiran, J. Li, and L. S. Wang (2003). *Nat. Mater.* **2**, 827.
- Q. Chen, W. L. Li, Y. F. Zhao, S. Y. Zhang, H. S. Hu, H. Bai, H. R. Li, W. J. Tian, H. G. Lu, H. J. Zhai, S. D. Li, J. Li, and L. S. Wang (2015). *ACS Nano* **9**, 754.
- H. J. Zhai, Y. F. Zhao, W. L. Li, Q. Chen, H. Bai, H. S. Hu, Z. A. Piazza, W. J. Tian, H. G. Lu, Y. B. Wu, Y. W. Mu, G. F. Wei, Z. P. Liu, J. Li, S. D. Li, and L. S. Wang (2014). *Nat. Chem.* **6**, 727.
- H. Bai, T. T. Chen, Q. Chen, X. Y. Zhao, Y. Y. Zhang, W. J. Chen, W. L. Li, L. F. Cheung, B. Bai, J. Cavanagh, W. Huang, S. D. Li, J. Li, and L. S. Wang (2019). *Nanoscale* **11**, 23286.
- T. Jian, X. N. Chen, S. D. Li, A. I. Boldyrev, J. Li, and L. S. Wang (2019). *Chem. Soc. Rev.* **48**, 3550.
- E. Oger, N. R. M. Crawford, R. Kelting, P. Weis, M. M. Kappes, and R. Ahlrichs (2007). *Angew. Chem. Int. Ed.* **46**, 8503.
- Y. J. Wang, X. Y. Zhao, Q. Chen, H. J. Zhai, and S. D. Li (2015). *Nanoscale* **7**, 16054.
- G. Martinez-Guajardo, A. P. Sergeeva, A. I. Boldyrev, T. Heine, J. M. Ugalde, and G. Merino (2011). *Chem. Commun.* **47**, 6242.
- M. R. Fagiani, X. W. Song, P. Petkov, S. Debnath, S. Gewinner, W. Schöllkopf, T. Heine, A. Fielicke, and K. R. Asmis (2016). *Angew. Chem. Int. Ed.* **55**, 1.
- Y. J. Wang, X. R. You, Q. Chen, L. Y. Feng, K. Wang, T. Ou, X. Y. Zhao, H. J. Zhai, and S. D. Li (2016). *Phys. Chem. Chem. Phys.* **18**, 15774.
- D. Moreno, S. Pan, L. L. Zeonjuk, R. Islas, E. Osorio, G. Martinez-Guajardo, P. K. Chattaraj, T. Heine, and G. Merino (2014). *Chem. Commun.* **50**, 8140.
- J. O. C. Jiménez-Halla, R. Islas, T. Heine, and G. Merino (2010). *Angew. Chem. Int. Ed.* **49**, 5668.
- T. B. Tai, A. Ceulemans, and M. T. Nguyen (2012). *Chem. Eur. J.* **18**, 4510.
- C. Romanescu, T. R. Galeev, W. L. Li, A. I. Boldyrev, and L. S. Wang (2011). *Angew. Chem. Int. Ed.* **50**, 9334.
- T. R. Galeev, C. Romanescu, W. L. Li, L. S. Wang, and A. I. Boldyrev (2012). *Angew. Chem. Int. Ed.* **51**, 2101.
- I. A. Popov, W. L. Li, Z. A. Piazza, A. I. Boldyrev, and L. S. Wang (2014). *J. Phys. Chem. A* **118**, 8098.
- T. Jian, W. L. Li, I. A. Popov, G. V. Lopez, X. Chen, A. I. Boldyrev, J. Li, and L. S. Wang (2016). *J. Chem. Phys.* **144**, 154310.
- I. A. Popov, T. Jian, G. V. Lopez, A. I. Boldyrev, and L. S. Wang (2015). *Nat. Commun.* **6**, 8654.
- T. Jian, W. L. Li, X. Chen, T. T. Chen, G. V. Lopez, J. Li, and L. S. Wang (2016). *Chem. Sci.* **7**, 7020.
- W. L. Li, T. Jian, X. Chen, H. R. Li, T. T. Chen, X. M. Luo, S. D. Li, J. Li, and L. S. Wang (2017). *Chem. Commun.* **53**, 1587.
- X. Y. Zhao, X. M. Luo, X. X. Tian, H. G. Lu, and S. D. Li (2019). *J. Clust. Sci.* **30**, 115.
- M. Yan, H. R. Li, X. Y. Zhao, X. Q. Lu, Y. W. Mu, H. G. Lu, and S. D. Li (2019). *J. Comput. Chem.* **40**, 966.
- M. Yan, H. R. Li, X. X. Tian, Y. W. Mu, H. G. Lu, and S. D. Li (2019). *J. Comput. Chem.* **40**, 1227.
- Y. Y. Ma, M. Yan, H. R. Li, Y. B. Wu, X. X. Tian, H. G. Lu, and S. D. Li (2019). *Sci. Rep.* **9**, 17074.
- W. L. Li, T. T. Chen, D. H. Xing, X. Chen, J. Li, and L. S. Wang (2018). *Proc. Natl. Acad. Sci. U. S. A.* **115**, E6972.
- T. T. Chen, W. L. Li, J. Li, and L. S. Wang (2019). *Chem. Sci.* **10**, 2534.
- T. T. Chen, W. L. Li, W. J. Chen, J. Li, and L. S. Wang (2019). *Chem. Commun.* **55**, 7864.
- T. T. Chen, W. L. Li, W. J. Chen, X. H. Yu, X. R. Dong, J. Li, and L. S. Wang (2020). *Nat. Commun.* **11**, 2766.
- X. Q. Lu, Q. Chen, X. X. Tian, Y. W. Mu, H. G. Lu, and S. D. Li (2019). *Nanoscale* **11**, 21311.
- X. Y. Zhao, M. Yan, Z. H. Wei, and S. D. Li (2020). *RSC Advances* **10**, 34225.
- X. Chen, Y. F. Zhao, Y. Y. Zhang, and J. Li (2019). *J. Comput. Chem.* **40**, 1105.
- C. Adamo and V. Barone (1999). *J. Chem. Phys.* **110**, 6158.
- J. Tao, J. P. Perdew, V. N. Staroverov, and G. E. Scuseria (2003). *Phys. Rev. Lett.* **91**, 146401.
- R. Krishnan, J. S. Binkley, R. Seeger, and J. A. Pople (1980). *J. Chem. Phys.* **72**, 650.
- D. Feller (1996). *J. Comput. Chem.* **17**, 1571.
- L. Schuchardt, B. T. Didier, T. Elsethagen, L. Sun, V. Gurmooorthi, J. Chase, J. Li, and T. L. Windus (2007). *J. Chem. Inf. Model.* **47**, 1045.
- M. J. Frisch, et al. (2009). Gaussian 09, Revision D.01, Gaussian, Inc., Wallingford, CT.
- J. Čížek (1969). *Adv. Chem. Phys.* **14**, 35.
- G. D. Purvis III. and R. J. Bartlett (1982). *J. Chem. Phys.* **76**, 1910.
- K. Raghavachari, G. W. Trucks, J. A. Pople, and M. Head-Gordon (1989). *Chem. Phys. Lett.* **157**, 479.
- H. J. Werner, et al. (2012). Molpro, version 1 (www.molpro.net).
- N. V. Tkachenko and A. I. Boldyrev (2019). *Phys. Chem. Chem. Phys.* **21**, 9590.
- E. D. Glendening, J. K. Badenhoop, A. E. Reed, J. E. Carpenter, J. A. Bohmann, C. M. Morales, C. R. Landis, and F. Weinhold (2013). NBO 6.0, Theoretical Chemistry Institute, University of Wisconsin, Madison.
- J. VandeVondele, M. Krack, F. Mohamed, M. Parrinello, T. Chassaing, and J. Hutter (2005). *Comput. Phys. Commun.* **167**, 103.
- T. Ziegler and A. Rauk (1977). *Theor. Chim. Acta* **46**, 1.
- M. P. Mitoraj, A. Michalak, and T. Ziegler (2009). *J. Chem. Theory Comput.* **5**, 962.
- M. Mitoraj and A. Michalak (2007). *Organometallics* **26**, 6576.

55. G. te Velde, F. M. Bickelhaupt, E. J. Baerends, C. Fonseca Guerra, S. J. A. van Gisbergen, J. G. Snijders, and T. Ziegler (2001). *J. Comput. Chem.* **22**, 931.
56. C. Chang, M. Pelissier, and P. Durand (1986). *Phys. Scr.* **34**, 394.
57. J. L. Heully, I. Lindgren, E. Lindroth, S. Lundqvist, and A. M. Martensson-Pendrill (1986). *J. Phys. B: At. Mol. Phys.* **19**, 2799.
58. E. V. Lenthe, E. J. Baerends, and J. G. Snijders (1993). *J. Chem. Phys.* **99**, 4597.
59. J. A. Dean (1999). *Lange's Handbook of Chemistry*, McGraw-Hill, New York, Table 4.6.

Publisher's Note Springer Nature remains neutral with regard to jurisdictional claims in published maps and institutional affiliations.